The evolution of the boundary layer in turbulent Rayleigh-Bénard convection in air

R. du Puits and C. Willert

Citation: Physics of Fluids **28**, 044108 (2016); doi: 10.1063/1.4947261
View online: http://dx.doi.org/10.1063/1.4947261
View Table of Contents: http://scitation.aip.org/content/aip/journal/pof2/28/4?ver=pdfcov
Published by the AIP Publishing

PHYSICS OF FLUIDS **28**, 044108 (2016)

The evolution of the boundary layer in turbulent Rayleigh-Bénard convection in air

R. du Puits[1,a] and C. Willert[2]
[1]*Institute of Thermodynamics and Fluid Mechanics, Technische Universitaet Ilmenau, P.O. Box 100 565, 98684 Ilmenau, Germany*
[2]*Institute of Propulsion Technology, German Aerospace Center, 51170 Koeln, Germany*

(Received 12 October 2015; accepted 31 March 2016; published online 29 April 2016)

We report measurements of the near-wall flow field in turbulent Rayleigh-Bénard convection in air ($Pr = 0.7$) using particle image velocimetry. The measurements were performed in a thin, rectangular sample at fixed Rayleigh number $Ra = 1.45 \times 10^{10}$. In particular, we focus on the evolution of the boundary layer that a single convection roll generates along its path at the lower horizontal plate. We identify three specific flow regions along this path: (i) a region of wall-normal impingement of the down flow close to one corner of the sample, (ii) a region where a shear layer with almost constant thickness evolves, and (iii) a region in which this boundary layer grows and eventually detaches from the plate surface at the opposite corner of the sample. Our measurements with a spatial resolution better than 1/500 of the total thickness of the boundary layer show that the typical velocity field as well as its statistics qualitatively varies between the three flow regions. In particular, it could be verified that the shear layer region covering about 75% of the total area of the plate is in transition to turbulence at the Rayleigh number as low as investigated in the present work. *Published by AIP Publishing.* [http://dx.doi.org/10.1063/1.4947261]

I. INTRODUCTION

The experimental evidence of the ultimate regime of convection in a laboratory experiment is one of the big challenges since Kraichnan's prediction in 1962.[1] In order to evaluate the onset of this regime, researchers usually check the criterion of the change of the exponent γ in the $Nu \sim Ra^{\gamma}$ power law (for the definition of Nu and Ra see below) which, however, provides inconsistent results at various experimental facilities.[2–6] In our work, we are taking up Kraichnan's original idea who linked the onset of the ultimate regime to a transition of the boundary layers from laminarity to turbulence and we characterize the velocity field adjacent to the horizontal plates in the transitional parameter domain.

Thermal convection is a physical phenomenon omnipresent in a great variety of technical and engineering applications as well as in our natural environment. A dimensionless quantity frequently used to describe its behavior is the Rayleigh number $Ra = (\beta g \Delta\vartheta H^3)/(\nu\kappa)$ with β being the thermal expansion coefficient, g being the gravitational acceleration, $\Delta\vartheta$ being the vertical temperature drop in the fluid across the vertical extent H. The variables ν and κ represent the properties of the fluid and stand for the kinematic viscosity and the thermal diffusivity. While many technical and engineering processes proceed at moderate Ra numbers below $Ra < 10^{14}$, the majority of environmental flows like those in the atmosphere or in the oceans feature much higher Ra numbers up to $Ra \approx 10^{20}$. The understanding of thermal convection in this parameter domain, that is commonly referred to as ultimate regime of convection, remains a challenge to scientists in physics, engineering, and meteorology. Most of the time, this problem is studied in the Rayleigh-Bénard (RB) setup, a fluid layer of thickness H that is heated from below and cooled from the top. In experiments,

[a]Electronic mail: ronald.dupuits@tu-ilmenau.de. URL: http://www.ilmenauer-fass.de.

the fluid layer is usually confined by sidewalls where the associated aspect ratio Γ – defined as the ratio between the lateral dimension and the thickness of the fluid layer H – becomes an important criterion that strongly affects the flow. The third dimensionless number completing the set of input parameters is the Prandtl number which is defined as $Pr = \nu/\kappa$.

The main question of the problem sounds very easy but is not yet answered satisfactorily: *How large is the heat flux throughout the fluid layer with respect to the input of the system?* Over many decades, it has become quite popular to express this in terms of a scaling law as $Nu = C\ Ra^{\gamma}$.[2,7–10] Here, the Nusselt number Nu is a dimensionless quantity which normalizes the total heat flux with respect to the diffusive heat flux. Various predictions of this scaling behavior have been proposed in the past, along with a great variety of those exponents. Without any claim of completeness, a few milestones should be mentioned here. Based on the principles of marginal stability and self-similarity of the boundary layers (the notation "boundary layer" is commonly used in the RB community for the flow field close to both horizontal plates in which the mean velocity and the mean temperature gradients differ from zero) and the assumption that they are fully decoupled, Malkus predicted an exponent $\gamma = 1/3$.[7,8] This model was completed by Kraichnan who predicted a transition of the boundary layers towards turbulence at a sufficiently high Rayleigh number.[1] Convection beyond this bound that is commonly referred to as the ultimate regime of convection, is characterized by an exponent $\gamma \to 0.5$ (with logarithmic corrections due to the viscous sub-layer). Later on, a group in Chicago running high Rayleigh number experiments in low temperature helium came up with the so-called mixing zone model that leads to an exponent $\gamma = 2/7$.[2] The same exponent was predicted by Shraiman and Siggia under the assumption that the boundary layers at the top and bottom plates are generally turbulent.[9] Based on a decomposition of the fluid layer in the well-mixed bulk region and the two boundary layers, Grossmann and Lohse predicted a comprehensive set of scaling functions $Nu = f(Ra,Pr)$ (and $Re = f(Ra,Pr)$) in their "Unifying theory of scaling in thermal convection."[10,11] One of the central ideas in their work is the hypothesis that the boundary layers are of laminar, though time-dependent Prandtl-Blasius type below a critical Ra number (classical regime) while they become turbulent beyond this bound (ultimate regime). With respect to the previous work of Kraichnan, they refined the prediction of the exponents and they fixed the critical Ra number at which the boundary layer transition occurs. A more recent but less known model by Hoelling and Herwig is based on an asymptotic consideration of the temperature field close to the top and bottom plates. The predicted correlation $Nu = f(Ra,Pr)$ was found to be in good agreement with data from highly accurate Rayleigh-Bénard experiments for Rayleigh numbers between 10^5 and 10^{15} and Prandtl numbers larger than 0.5. Almost all of these theories are based essentially on boundary layer models and, therefore, a great effort has been spent over the last years to characterize the velocity and the temperature fields in the flow region adjacent to the walls.

Although a great number of various Rayleigh-Bénard experiments exist, only a few configurations meet the criteria to give insight into this specific flow region: (i) a sufficiently high Rayleigh number, (ii) measurement access to the velocity *and* the temperature field, and (iii) a measurement technique that is capable to resolve the fine structure of the near-wall flow field. To the authors' knowledge, there are only two facilities in the world that fulfill all requirements to measure the velocity field in the near-wall flow region with a sufficiently high resolution to discriminate between various predictions: The $81 \times 20 \times 76$ cm^3 water cell at The Chinese University of Hong Kong[12] and the Barrel of Ilmenau, 6.30 m in height and 7.15 m in diameter in which air is used as working fluid.[13] In both the facilities, Rayleigh numbers as high as $Ra = 10^{12}$ are feasible and the spatial resolution of the velocity measurement technique used is better than one-tenth of the total boundary layer thickness. However, it is important to mention here that the Prandtl numbers differ by roughly a factor of seven (for water $Pr \approx 5$, for air $Pr = 0.7$) and, in particular, the laminar-turbulent transition of the boundary layers may depend on that number. As reported in previous work by du Puits *et al.*,[14] this transition can be triggered by three different mechanisms: (i) a sufficiently large shear stress within the boundary layer,[15,16] (ii) the entrainment of turbulent kinetic energy from the bulk, and (iii) buoyancy forces inside the boundary layer due to a strong wall-normal temperature gradient.[17] While in case of high Prandtl numbers, the contribution of the latter effect vanishes (the strong temperature gradient appears only in the very inner part of the viscous boundary layer), this must be considered at low Prandtl numbers. However, measurements in the Hong

Kong water cell show a deviation of the profile of the mean horizontal velocity from that of a flat plate laminar shear layer which can only be brought into a good coincidence applying a dynamical re-scaling method with respect to the instantaneous thickness of the boundary layer.[18] Direct numerical simulations (DNSs) reported in the same paper basically confirm this result even though they are carried out in a two-dimensional domain. Three-dimensional velocity measurements in air using Laser Doppler Anemometry (LDA) that have been carried out in the large-scale RB experiment "Barrel of Ilmenau" ($Pr = 0.7$) also show a discrepancy between the measured velocity profiles and Prandtl's prediction of a laminar shear layer independent on a variation of the Rayleigh number ($3 \times 10^9 < Ra < 10^{12}$) or the aspect ratio ($1.13 < \Gamma < 11.3$).[19,20] This discrepancy was confirmed in DNS reported by van Reeuwijk *et al.*[21] and Scheel *et al.*[22] Even the application of the dynamical re-scaling does not lead to a collapse of the profiles with the prediction at Prandtl numbers as low as that of air.[23]

The aim of the work reported here is to give an insight into the boundary layer flow field in the parameter domain of Rayleigh numbers close to the transition towards the ultimate regime of convection. We provide a comprehensive set of particle image velocimetry data characterizing the velocity field at various locations along the path of the large-scale circulation in a quasi-two-dimensional rectangular RB cell. The paper is organized in the following way: Section II describes the experimental facility, the setup and the measurement technique. In Section III we discuss the flow field at the center of the heating plate and in Section IV, the evolution of the boundary layer along the horizontal extent of the heating plate and the consequences on the local heat transport coefficient are discussed.

II. EXPERIMENTAL SETUP AND MEASUREMENT TECHNIQUE

A. The large-scale Rayleigh-Bénard experiment "Barrel of Ilmenau"

The experimental work has been done in a large-scale Rayleigh-Bénard experiment that is referred to as the "Barrel of Ilmenau" (www.ilmenauer-fass.de). The sample shown in a sketch in Fig. 1 is of cylindrical shape with an inner diameter of $D = 7.15$ m and a total height of 8.00 m. It is filled with ambient air having a Prandtl number of $Pr = 0.7$ being virtually independent on temperature. The air is confined between a hot plate at the bottom, a free hanging cold plate at

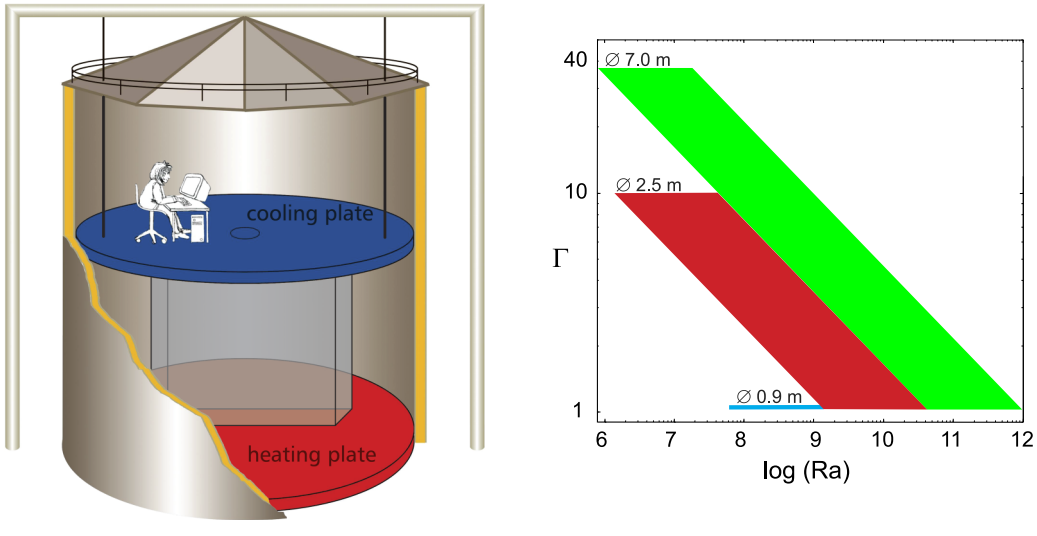

FIG. 1. Sketch of the large-scale Rayleigh-Bénard experiment "Barrel of Ilmenau" with the rectangular sample inside (left inset). The entire parameter domain achievable in the big barrel ($D = 7.0$ m) and using various insets ($D = 2.5$ m, $D = 0.9$ m) is shown in the Ra–Γ phase space (right inset). The measurements reported herein were undertaken in a rectangular sample at a fixed Rayleigh number $Ra = 1.45 \times 10^{10}$ and aspect ratios $\Gamma_x = 1$ and $\Gamma_y = 0.25$.

the top as well as an adiabatic cylindrical sidewall. The distance between both plates that corresponds to the thickness of the air layer can be set between $H = 0.20$ m and $H = 6.30$ m covering a wide aspect ratio range of $1.1 < \Gamma < 36$. Both plates are carefully designed to ensure the boundary condition of uniform temperature. To this end, the heated bottom plate consists of two separate parts: an electrical underfloor heating system embedded in a concrete layer of 5 cm thickness that is isolated towards the ground below with polyurethane plates of 0.3 m thickness. At the upper side of the concrete layer, an aluminum overlay of 37 mm thickness is placed in which water circulates. It is separated into an inner circle of 0.95 m diameter and 24 outer, cake slice like segments arranged around the inner circle. The heating power generated in the underfloor heating system is transferred into the overlay via a 2 mm pad of silicone. The water circulation inside the overlay ensures a uniform temperature distribution at the surface of the hot plate and balances the differences of the convective heat flux at the plate-air interface. The free-hanging cooling plate consists of 16 segments with a water circulation inside as well. The segments are mounted on a solid steel construction and are separately leveled perpendicular to the vector of gravity. The entire construction with a weight of about 6 tons is mounted on a crane and can be lifted up and down. The temperature of the hot and the cold plates, respectively, can be set in a range $15\,^{\circ}\mathrm{C} < T_h < 80\,^{\circ}\mathrm{C}$ and $5\,^{\circ}\mathrm{C} < T_c < 30\,^{\circ}\mathrm{C}$. The maximum deviation of any local temperature at the surface of the hot plate is typically less than ±1% of the total temperature difference between the plates (±1.5% at the cold plate). Over time, the mean temperature at the surface of both plates varies no more than ±0.02 K. The entire parameter domain in the $Ra - \Gamma$ phase space that can be controlled by the settings of the temperature difference $\Delta\vartheta$ and the thickness of the fluid layer H is indicated in Fig. 1.

In order to ensure the adiabatic boundary condition at the sidewall, that means to inhibit the heat exchange between the confined air within the sample and the air in the environment, an active compensation heating system is installed. Electrical heating elements are placed in between the 16 cm inner and the 12 cm outer isolation of the sidewall. The temperature of each of the 18 heating panels around the cell is controlled in such a way that the temperature of the panel is kept equal to the temperature at the inner side of the insulating layer. As long as the temperature inside the RB cell does not fall below the ambient temperature, this system effectively prevents the heat exchange through the sidewall. We have checked the heat loss of the test sample by setting the temperature of both plates to 30 °C and found it to be smaller than 0.5% of the total convective heat transport between the bottom and the top plates.

B. Setup of the PIV measurement technique

Measurements of the near-wall flow field in turbulent Rayleigh-Bénard convection in a cylindrical test cell would generally require a fully 3d measurement technique, since the plane of the large-scale circulation (LSC) that drives the shear layer at the plate surface underlies very complex variations in space and time.[24–26] In order to simplify the problem and to use a single-camera setup for the particle image velocimetry measurements (PIV), we fix the LSC in a single plane by confining it in a rectangular box of dimensions $2.50 \times 2.50 \times 0.62$ m^3 (width × height × depth) corresponding to aspect ratios $\Gamma_x = 1$ and $\Gamma_y = 0.25$ in x- and y-direction, respectively. The box is made of transparent Perspex and was placed inside the large RB cell using its original heating and cooling plates as bottom and top walls (see Fig. 1). The temperature difference across the fluid layer was fixed at $\Delta\vartheta = 10$ K yielding a Rayleigh number $Ra = 1.45 \times 10^{10}$. At the sidewall of the rectangular box the adiabatic boundary condition is given by default since the vertical temperature fields inside and outside the box are virtually equal.

A laser light sheet illumination according to Fig. 2 was realized using a 2 W continuous wave laser in combination with a system of cylindrical lenses, mirrors, and apertures. The particular challenge of the setup was to align the laser light sheet as close as possible to the surface of the 2.5 m long heating plate with minimal reflection from the polished aluminium plate which would introduce interference lines into the light sheet. The height of the light sheet was 70 mm along the total width of the cell. At its waist, the light sheet thickness is about 1 mm and increases to approximately 2 mm at either end of the RB cell. As shown in Fig. 5, precise measurements in this setup were feasible up to a minimum surface distance of about $z = 0.5$ mm. A smoke generator,

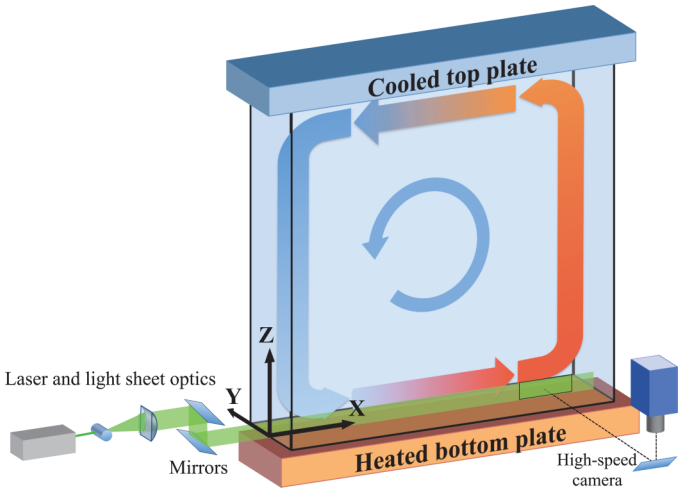

FIG. 2. Setup of the particle image velocimetry technique measuring the near-wall flow field at the hot bottom plate.

based on an evaporation-condensation principle, was used to seed the flow with 1–2 μm oil droplets whose lifetime exceeds 1 h. After filling/refilling the box, we wait at least 15 min before we start an acquisition of PIV image sequences.

Images of the illuminated particles were acquired with a high-speed camera (PCO GmbH, Dimax-S4) at a frame rate of 200 Hz and a spatial resolution of 2016×600 pixels. The camera was arranged in front of the light sheet in an upright position. Using a 45° mirror in front of the macro-lens (Zeiss Macro-Planar 100/2), the optical axis was aligned normal to the light sheet. The complete imaging setup could be traversed along the x-direction to capture the spatial development of the flow within the cell. The exposure time was chosen to 2 ms to minimize particle streaking by the continuous laser illumination. Aside from its high light sensitivity, the main benefits of the chosen camera are its large dynamic range of 12 bits and large internal memory to capture continuous sequences of more than 20 000 frames at the chosen frame rate. Various image sequences at two magnifications were captured, the smaller one to obtain the global features of the boundary layer and the larger, and the higher resolved one to retrieve selected profiles with an improved statistical convergence. An overview of the imaging parameters for the acquired PIV sequences is given in Table I.

III. RESULTS

A. The flow field at the center of the plate

In this section, we will focus our discussion on the flow field at the center of the plate. At this location, the orientation of the large-scale circulation is from left to right and the streamlines of the time-averaged flow field are aligned parallel to the wall. Analogous to a shear flow along a

TABLE I. Imaging parameters for the acquired PIV sequences of near wall RB convection.

	Symbol	Overview	Detailed view A, B, C, D	Unit
Magnification	m	9.1	22.1	pixel/mm
Field of view	$[W \times H]$	220×65	13×68	mm^2
	$[W \times H]$	2016×600	288×1500	pixel
Camera frame rate	f_{acq}	200	100/200	Hz
Camera exposure time	t_{exp}	2.0	2.0	ms
Duration	t_{seq}	106	592/296	s
Number of frames	N	21 161	59235	

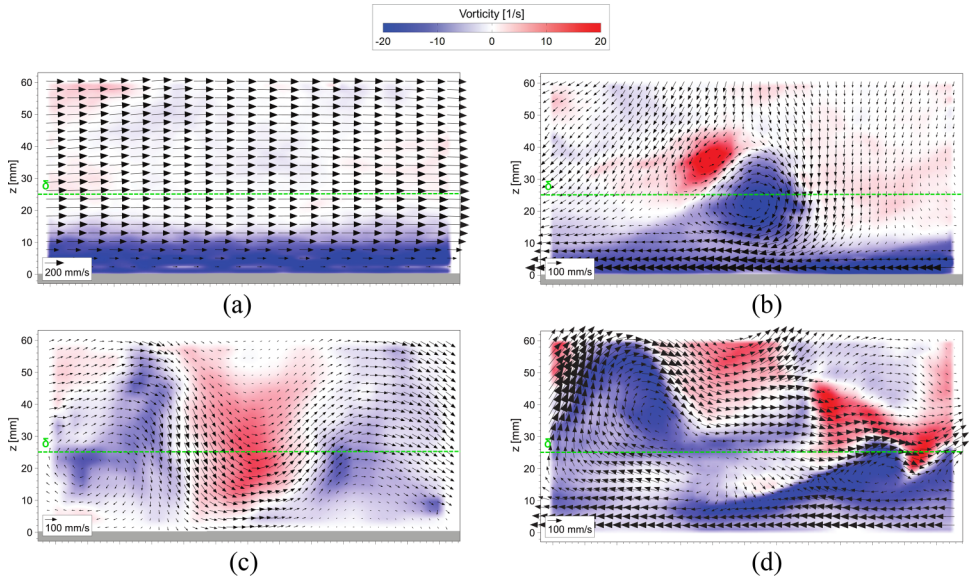

FIG. 3. Various instantaneous flow states at the center of the heating plate: (a) a laminar flow phase, (b) a transitional flow phase due to the inner shear of the boundary layer and thermal instabilities within it, (c) a transitional flow phase due to the entrainment of turbulent kinetic energy from the large-scale circulation, (d) a fully turbulent flow phase. The flow phases alternate within a few seconds. The position of the time-averaged boundary layer thickness $\delta_{99} = 25.3$ mm is indicated as well. Please note that for clarity, the mean wind is subtracted from the velocity fields shown in the two right subfigures.

flat plate, the flow within the cell develops a boundary layer. In order to give the reader an idea on the complexity and the dynamics of such a boundary layer in turbulent RB convection even at moderate Rayleigh numbers, we have added a movie as the supplementary material.[27] The movie running with 50% of the originally captured frame rate shows the flow field in a wall-normal plane. The visible area is about 250 mm in width and 70 mm in height corresponding to 2–3 times the thickness of the kinematic boundary layer. The exposure time is chosen as long as required to capture trajectories of the injected particles. Through visual analysis of the sequence, the following four characteristic flow phases could be identified as shown in the four snapshots of the velocity/vorticity fields in Fig. 3:

- a laminar flow phase (right at the beginning of the sequence),
- a transitional flow phase due to the inner shear of the boundary layer and thermal instabilities within it,
- a transitional flow phase due to the entrainment of turbulent kinetic energy (coherent structures) from the large-scale circulation,
- a fully turbulent flow phase (at the end of the sequence).

Fig. 3(a) shows the instantaneous velocity field along with the out-of-plane vorticity component ω_y obtained during a laminar flow phase. The wall-normal velocity component essentially vanishes and the vorticity field is weak except very close to the plate surface where a strong gradient is present. Clearly, there is no indication of turbulence. After a few seconds, the boundary layer becomes unstable. Shear induced instabilities such as Kelvin-Helmholtz waves as well as buoyancy induced instabilities like thermal plumes develop and disturb the laminar stratification of the near-wall flow field. A typical example of a buoyancy driven instability, a mushroom-like plume is shown in Fig. 3(b). Those instabilities, however, are only one trigger to induce turbulence in the boundary layer. Another way to mix the boundary layer becomes visible proceeding with the video sequence. Roughly at second 25, a large vortex enters the field of view from the left. That vortex, much larger than the dimension of the boundary layer was most likely generated in the turbulent bulk region of the RB cell and has been carried by the LSC. In this specific instant here, the vortex structure penetrates deeply into the boundary layer and it even generates a back flow as shown in Fig. 3(c).

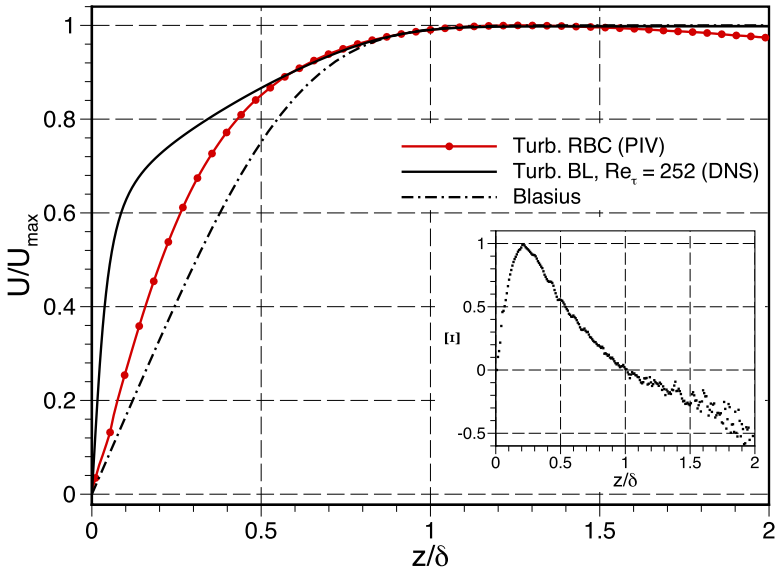

FIG. 4. Profile of the time-averaged horizontal velocity at the center of the heating plate (red dots) along with the prediction for a laminar boundary layer according to Prandtl/Blasius (dashed-dotted line) and a fully turbulent boundary layer at $Re_\tau = 252$ (fully black line, DNS by Schlatter *et al.*[29]). The inset shows the diagnostic function $\Xi = d(U/U_{max})/d(\log(z/\delta))$.

In the last seconds of the video sequence, the flow field looks, at least by eyes, fully turbulent inside and outside the boundary layer before re-laminarizing at the very end of the sequence. What is remarkable is that all four characteristic flow phases could be observed within a very short period of only 22 s (please note that the speed of the video sequence is reduced by a factor of two with respect to the original one). The permanent alteration between laminar, transitional, and fully turbulent flow phases is referred to as intermittency and has been found as a typical feature of the near-wall flow field in turbulent RB convection even at a Rayleigh number as low as $Ra = 1.5 \times 10^{10}$.[14] In order to characterize this particular state of the boundary layer in a more quantitative way, we performed a series of PIV measurements as already described in Section II B.

First of all, we show the profile of the mean horizontal velocity $U(z)$ at the center of the heating plate. In Fig. 4 the measured profile is plotted along with the prediction of a pure laminar boundary layer according to Prandtl/Blasius[28] and a fully turbulent boundary layer obtained from a direct numerical simulation at $Re_\tau = 252$ (Re_τ–Reynolds number based on the wall friction velocity).[29] In order to fit the various profiles, the 99% criterion of the asymptotic velocity of the outer flow was chosen as a reference point. In our eyes, this is a more reliable way to interpret the measured velocity profile with respect to a laminar or a turbulent boundary layer than the usually used criterion of the slope of the near-wall velocity. It is quite obvious that our data neither collapse with the prediction of a laminar boundary layer nor with the numerical data of the fully turbulent one. The measured profile of the mean horizontal velocity in turbulent RB convection in air lies in between the two, which clearly confirms the transitional character of the boundary layers. Moreover, we have checked the profile with respect to a logarithmic functionality as expected for a fully turbulent boundary layer. We computed the diagnostic function $\Xi = d(U/U_{max})/d(\log(z/\delta))$ and plotted the result in the inset of Fig. 4. In case that the curve or any fraction of the curve would correspond to a logarithmic function, a plateau should be visible. However, there is none, meaning that the full turbulent state is not yet approached.

Another characterizing quantity of the boundary layer is the wall shear stress. It is directly linked to the wall shear rate (or the velocity gradient at the wall) $\dot{\gamma} = dU/dz$ by the following expression:

$$\tau_w = \mu \frac{dU}{dz}\Big|_{z=0}. \tag{1}$$

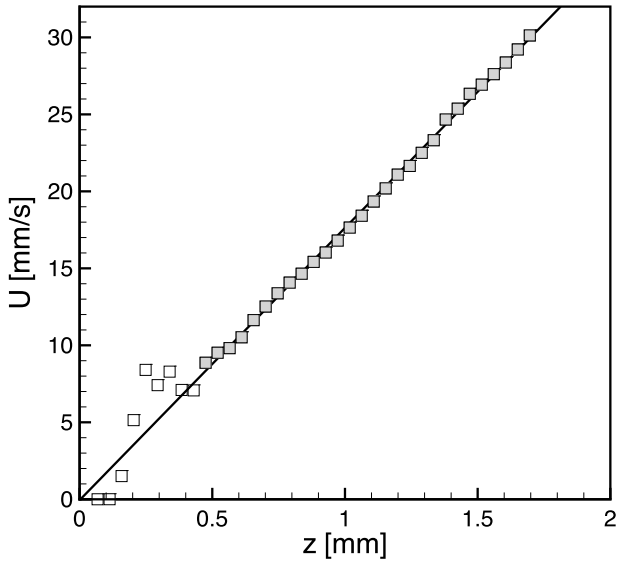

FIG. 5. Highly resolved profile of the mean velocity in the viscous sublayer obtained by single-line image cross-correlation.

In order to recover estimates of the wall shear stress using particle based imaging methods, it is required that the linear portion of the sublayer is sufficiently well resolved. In that case, the gradient can be obtained through finite differences of velocity estimates. Within the linear region, the fluid motion and along with it the motion of the particles is wall parallel. Therefore it is possible to limit the frame-to-frame displacement estimation to recover only the wall parallel motion. With the camera properly aligned, this can be achieved by cross-correlating single rows of wall-parallel pixels. Fig. 5 shows the mean of the stream-wise velocity component u of the flow field within 30 pixels from the wall. Aside from deviations really close to the wall, caused by stationary particles or dust sticking at the surface, the profile is linear throughout owing to the nearly 5 mm thick viscous sublayer of the RB convection boundary layer. The slope of a linear fit to this linear fraction of the profile provides an estimate of the wall shear rate $\dot{\gamma}_w = dU/dz\big|_{z=0}$ and can be used for the straightforward calculation of the friction velocity U_τ and the wall unit z^+/z. For a value of $\dot{\gamma}_w = 17.95\ \mathrm{s}^{-1}$ deduced from Fig. 5, this yields

$$U_\tau = \sqrt{\frac{\tau_\mathrm{w}}{\rho}} = \sqrt{\nu \frac{dU}{dz}\Big|_{y=0}} = 17.1\ \mathrm{mm/s}, \tag{2}$$

$$\frac{z^+}{z} = \frac{u_\tau}{\nu} = 1.05\ \mathrm{mm}^{-1}. \tag{3}$$

Since it had become quite popular in the past to associate the wall shear rate with the boundary layer thickness — frequently, it is defined as the crossover between the linear extension of the velocity gradient $dU/dz\big|_{z=0}$ and the asymptotic velocity outside the boundary layer U_inf – we will briefly discuss the temporal evolution of that quantity. We plot a time series of the instantaneous wall shear rate over a period of 60 s and the corresponding probability density function (PDF) in Fig. 6. In this short but representative sequence, the wall shear rate strongly fluctuates around its mean of $\dot{\gamma}_w = 13.7\ \mathrm{s}^{-1}$ and achieves values of $\dot{\gamma}_w = 37\ \mathrm{s}^{-1}$ as well as $\dot{\gamma}_w = 0\ \mathrm{s}^{-1}$. At time $t = 104$ s, even a negative shear rate appears meaning that the flow locally reverses, such as observed in Fig. 3. The transitional but not fully turbulent character of the boundary layer becomes also visible analyzing the PDF of the fluctuations of the wall shear rate. Their distribution is slightly skewed towards positive fluctuations and looks quite similar to a fully turbulent boundary layer (see inset of the right inset of Fig. 6) though the skewness of the present flow is less pronounced.

The profiles of the velocity fluctuations $|u'|$ (parallel to the wall) and $|w'|$ (normal to the wall) are shown in Fig. 7. Both quantities are normalized by the maximum of the mean horizontal velocity U_{max} and plotted versus z/δ. The fluctuations of the horizontal velocity component quickly grows

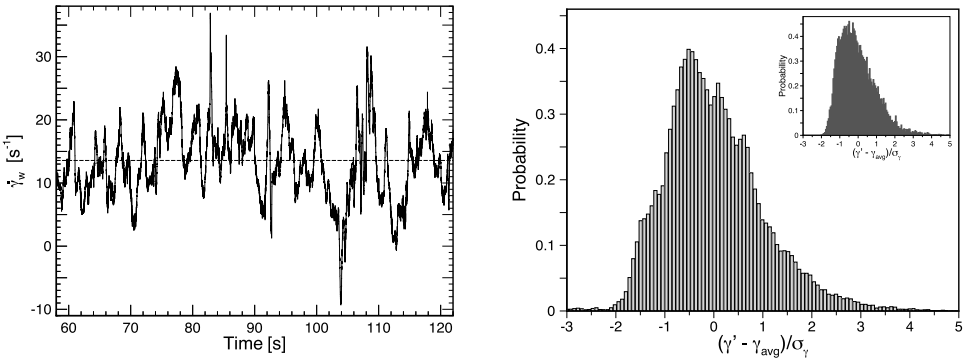

FIG. 6. Temporal evolution (12 000 samples, left inset) and probability density function (right inset) of the wall shear rate $\dot{\gamma}_w = dU/dz|_{z=0}$ at $x/L = 0.64$ (mean: 13.7 s^{-1}, σ : 6.8 s^{-1}, skewness: 0.51). The inset of the right inset shows the PDF of a fully turbulent boundary layer at $Re_\delta = 23\,000$ measured at the 1 m Goettingen Windtunnel.[30]

with the distance from the plate surface and approach their maximum already inside the boundary layer at $z/\delta \approx 0.6$. Beyond that maximum, the amplitude of the horizontal velocity fluctuations starts to decrease and converges with the curve of the wall-normal fluctuations at $z/\delta \approx 2$. This indicates increasing isotropy of turbulence with increasing wall distance. Compared with a DNS of a fully turbulent boundary layer (tbl) at $Re_\tau = 252$ (see Fig. 3 in Schlatter *et al.*[29]), our profiles are closer to that DNS than to a laminar boundary layer where the wall-normal fluctuations $|w'|$ completely vanish. Considering, e.g., the position $z/\delta \approx 0.6$, the wall normal fluctuations in the RB boundary layer amounts to $|w'| = 0.35|u'|$, not very far from the DNS of the tbl where the ratio is $|w'_{tbl}| = 0.47|u'_{tbl}|$. At larger distances, e.g., $z = 2\delta$, the ratios are $|w'| = 0.68|u'|$ (RB) and $|w'| = 0.66|u'|$ (tbl). Our experimental results are also in very good agreement with previously published DNS by van Reeuwijk *et al.*[21] who found the same behavior. The smaller amplitude of the fluctuations with respect to the maximum of the mean velocity in the DNS is possibly due to the higher Rayleigh number of our experiment since the DNS data exhibit a clear tendency that the fluctuations decrease with increasing Rayleigh number. The time-averaged Reynolds stress component $|u'w'|$ remains negative between the surface of the plate and the point $z = \delta$ at which the mean velocity approaches its maximum. The quantity gets close to zero near this point and increases to positive values beyond the edge of the boundary layer. This behavior is also similar to a tbl as discussed in Schlatter *et al.*[29] The little kink

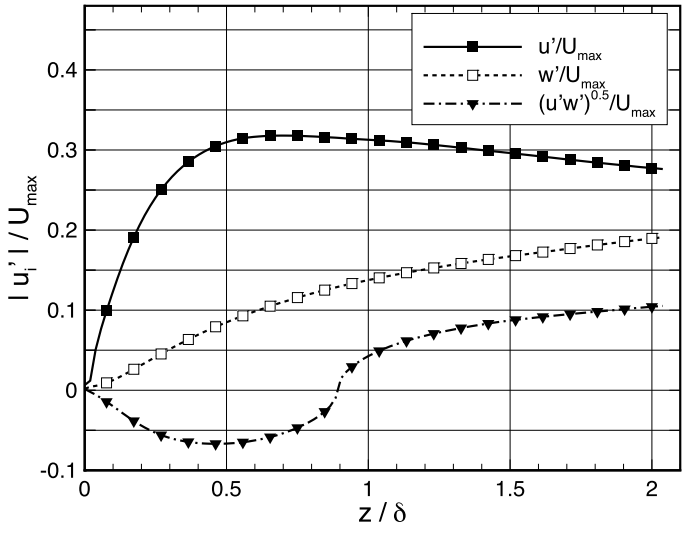

FIG. 7. Profiles of the velocity fluctuations $|u'|$, $|w'|$ and the time-averaged Reynolds stress $(u'w')^{0.5}$ normalized by the maximum velocity at the center of the heating plate.

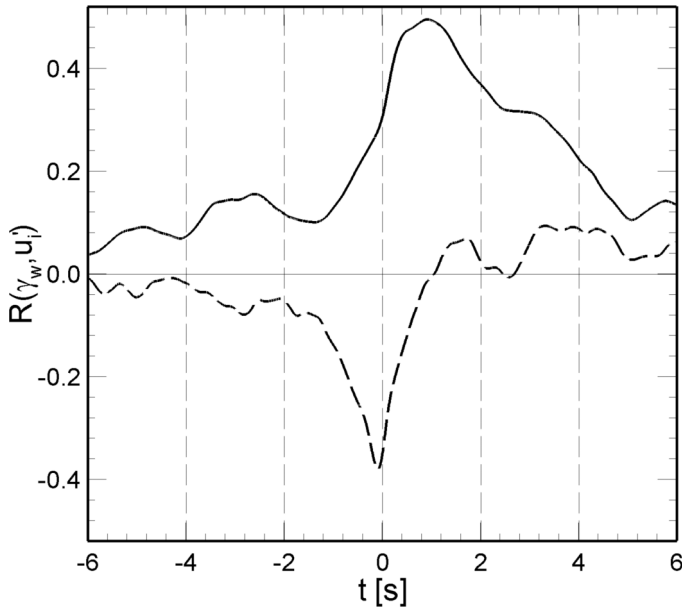

FIG. 8. Cross-correlation functions $R(\dot{\gamma}_w, u')$ (——) and $R(\dot{\gamma}_w, w')$ (- - -) between the wall shear rate $\dot{\gamma}_w$ and the velocity fluctuations u' and w' for a relative wall distance $z/\delta = 1$ at position $x/L = 0.64$.

of the curve at $z/\delta = 0.9$ might be an artefact of the PIV measurements that is visually amplified due to the specific representation of the square root of the quantity.

At the end of this section, we will try to answer the question: How strong is the interaction of the flow between the outer edge of the boundary layer and the fluid layer very close to the plate surface. To this end, we compute the correlation functions $R(\dot{\gamma}_w, u')$ and $R(\dot{\gamma}_w, w')$ between the instantaneous wall shear rate $\dot{\gamma}_w$ and the velocity fluctuations u' and w' at the edge of the boundary layer. The results are plotted in Fig. 8. For both velocity components, a clear correlation exists. The coupling is essentially caused by coherent structures carrying heat and momentum across the boundary layer. As shown in Fig. 3, those structures may appear as shear/thermal instabilities of the boundary layer itself or they are transported within the LSC and penetrate into the boundary layer almost touching the surface of the heating plate. In both cases, they enhance the local heat transfer coefficient with respect to the pure diffusive case.

B. The evolution of the boundary layer along the path of the mean wind

The canonical Rayleigh–Bénard problem that is generally under consideration in theory is defined as a fluid layer of infinite extent. In that problem, an infinite number of convection cells exist side by side and the flow field is not affected due to the existence of a sidewall. This specific scenario justifies to neglect the influence of the shape of the sample and in that case, the total heat transport only depends on Ra and Pr. In experiments, sidewalls are necessary to confine the fluid and the heat within the cell. Until now there is no conclusive bound of Γ at which the heat transport can be considered as that of an infinitely extended fluid layer. Recent numerical simulations indicate an asymptotic behavior at $\Gamma = 8$ but this could be verified only up to $Ra \approx 7 \times 10^7$.[31] However, the majority of RB experiments at ultra-high Rayleigh numbers are conducted in RB cells of much smaller aspect ratios $\Gamma \leq 1$ and according to the numerical results, the heat transport may differ up to 15% with respect to the infinite case. In those small aspect ratio cells, only a single convection roll or a vertical stack of convection rolls exist and the local flow field at the surface of the horizontal plates varies with respect to the location at the horizontal plates.[32,33] Hence, the local heat transfer coefficient varies as well (up to 30%) as shown by Kaiser and du Puits.[34] We present highly resolved particle image velocimetry measurements of the near wall flow field along the path of the mean wind at the heating plate. In our geometry of aspect ratios $\Gamma_x = 1$ and $\Gamma_y = 0.25$, the height

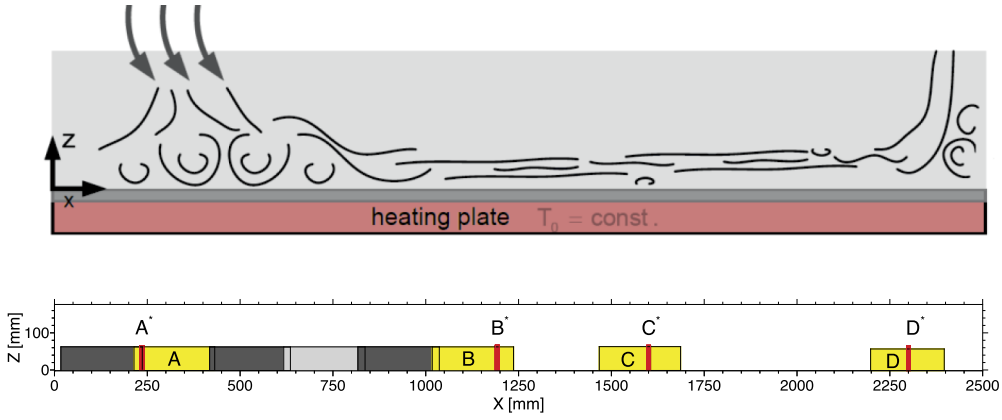

FIG. 9. Caricature of the typical evolution of the flow field along the path of the mean wind (upper inset) and PIV measurement positions at the heating plate (lower inset).

and the width are the same and due to the small depth, a single convection roll recirculates in a fixed plane as sketched in Fig. 2. Starting in the upper right corner of the cell, heated air arrives from the heated bottom plate. It gets deflected by 90° and becomes cooler along its passage along the (cold) top plate. Arriving at the left sidewall, the air is deflected downward by 90°, moves down and impinges the (hot) bottom plate similar to a free jet. Due to the confining sidewall on the left the flow is redirected to the right and starts to evolve a horizontal shear layer where the air is heated up again while passing along the bottom (heated) plate. Arriving at the opposite (right) sidewall, another 90° turn of the mean flow occurs and a secondary flow structure develops in the corner. A scheme, how this process qualitatively proceeds at the heated bottom plate is shown in Fig. 9.

In the following, we will characterize the flow field near the heated bottom plate at various locations along the path of the mean wind. To this end, we extended our PIV measurements above the center of the heating plate towards the entire left half of the plate surface 0 mm $< x/L <$ 0.5 and to selected areas at the right side of the plate $0.586 < x/L < 0.674$ and $0.879 < x < 0.959$. A complete overview of all measurement positions is shown in Fig. 9. Rectangular areas mark full frame PIV measurements with the maximum resolution of 2016×600 pixels and a duration of 106 s. In our discussion below, we focus on those areas marked in yellow which are representative of the three flow regions indicated below. The four narrow (red) stripes indicate positions that were imaged with higher spatial resolution and an extended duration of 296 s. The details of the measurements are listed in Table I (Section II B). From visual observation, the surface of the heating plate can be discriminated into the following three areas (starting from the left sidewall):

- Flow region 1: Impingement of the cold jet from the cooling plate,
- Flow region 2: Shear boundary layer along the plate surface,
- Flow region 3: Deflection of the flow at the right sidewall with secondary flow structures.

According to these three flow regions, vectors and streamlines of the mean velocity field along with the mean vorticity at selected measurement positions A, C, and D are plotted in Fig. 10. The upper inset shows the near-wall flow field in flow region 1. The streamlines are mainly aligned towards the surface of the horizontal plate. Due to the almost wall-normal impingement of the free stream at the plate surface, the flow field becomes well mixed. It is characterized by strong fluctuations (to be discussed below) and a strong vorticity that enhance the local heat transfer coefficient with respect to a classical shear layer. In analogy to the work of Shishkina *et al.*[33], we determine the size of that surface area using the point of vanishing wall shear stress. It is found at the position $x/L \approx 0.132$ which means that about 13% of the total plate surface is exposed to that flow condition in a rectangular sample at the given Ra number of $Ra = 1.45 \times 10^{10}$. Measurements of the local heat flux at the surface of the heating plate using an infrared camera indeed show that the local wall heat flux in flow region 1 is more than 30% higher than the heat flux at the center of the plate which is exposed to the shear layer.[35] While in flow region 2 a shear layer with

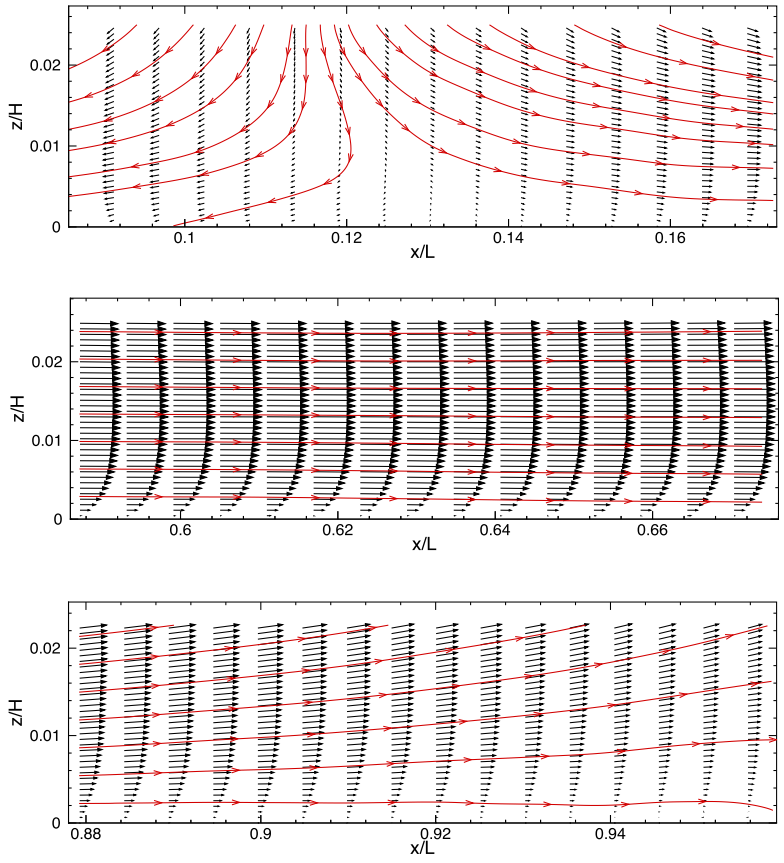

FIG. 10. Vector field and streamlines of the mean velocity field at measurement positions A (upper inset), C (middle inset), and D (lower inset), along with the mean vorticity field.

almost constant thickness evolves (already discussed in Section III A) the streamlines diverge in flow region 3 and the thickness of the boundary layer becomes thicker and thicker. Eventually, a vortex is generated in the lower right corner of the sample that also enhances the local heat transfer coefficient. The corner vortex is not visible in our plots since measurements at $x/L > 0.960$ are interfered by scattered light from the right sidewall through which the laser light sheet has been conducted. However, measurements of the local heat flux show as well an enhancement by about 10%–15%. Briefly summarized, the flow in flow region 1 ($0 < x/L < 0.132$) is clearly dominated by downward motion and even reverses with a clearly visible stagnation point at $x/L \approx 0.132$. In flow region 2 ($0.132 < x/L < 0.880$), the flow accelerates establishing a boundary layer of almost constant thickness $\delta \approx 30$–35 mm with a maximum velocity of $U_{max} \approx 160$–170 mm/s. Toward the right corner the mean streamlines diverge and indicate the deflection of the horizontal shear flow towards the upper plate by the vertical sidewall.

In order to analyse the near wall flow field in the those flow regions in more detail, extended series of images with enhanced magnification have been acquired at the positions A*, C*, and D* marked with the narrow (red) stripes in Fig. 9. Each of these series contains 59 235 images covering 296 s or about three large scale eddy turn over times. The characteristic values of the extended measurements of the near-wall flow field are summarized in Table II. Before we start our discussion, we wish to remind the reader that those quantities in column A* are only listed for completeness. There is no boundary layer in the classical sense and, thus, the data are not comparable with the ones at the positions B*, C*, and D*. While in the flow regions 2 and 3 the flow field fits the shear layer model quite well, in flow region 1 the streamlines are aligned towards the plate surface implying that an impinging jet model would be the better choice to describe the flow and the local heat transport near the left sidewall. The numbers in Table II confirm that the boundary layer

TABLE II. Boundary layer data obtained for measurement positions A* through D*.

		A*	B*	C*	D*	Unit
Position	x/L	0.09	0.48	0.64	0.92	...
Boundary layer thickness	δ_{Umax}	22.8	32.8	35.8	62.9	mm
Boundary layer thickness	$\delta_{99\%}$	18.7	25.3	27.7	51.3	mm
Kinematic boundary layer thickness	δ_ν	8.1	9.8	10.9	21.6	mm
Displacement thickness	δ_*	5.3	6.8	7.5	14.3	mm
Momentum thickness	δ_Θ	2.5	3.1	3.5	6.1	mm
Shape factor	$S=\delta_*/\delta_\Theta$	2.14	2.22	2.18	2.34	...
Maximum velocity	U_{max}	−37.8	169.0	155.0	83.2	mm/s
Wall shear rate	$\dot{\gamma}_w = dU/dz\big\|_{z=0}$	−3.8	16.7	13.7	2.8	1/s
Friction velocity	U_τ	−7.9	16.4	14.9	6.8	mm/s
Wall unit	z^+/z	0.486	1.015	0.920	0.419	1/mm
Shear Reynolds number	$Re_{\delta_{Umax}}$	(53.2)	343	343	323	...
Shear Reynolds number	$Re_{\delta_{99}}$	(43.8)	264	265	263	...
Shear Reynolds number	Re_{δ_ν}	(18.8)	103	104	111	...

thickness remains almost constant in flow region 2, regardless of which the definitions are used. In flow region 3, the boundary layer rapidly grows with decreasing distance from the right sidewall. At the position $x/L = 0.92$, it is almost twice as thick as at the center of the plate. The thickening of the boundary layer towards the right sidewall has also a bearing on the maximum velocity U_{max}, the friction velocity U_τ, the wall shear rate $\dot{\gamma}_w = dU/dz\big|_{z=0}$, and the size of the wall unit z^+/z which decreases accordingly. However, the shear Reynolds number stays virtually constant. This indicates that the boundary layer does not receive additional momentum from the outer flow aside from the momentum added by the down-welling fluid in flow region 1 ($x/L < 0.132$).

Finally, we will compare the strength of the mixing of the near-wall fluid layer being an indirect measure for the local heat transfer coefficient. This can be done by plotting the profiles of the fluctuations $|u'|$, $|w'|$ and the Reynolds stress $|u'w'|$. In order to give the reader an idea as well on the variation of those quantities with respect to the position x/L as the thickness of the mixing layer, we normalize the fluctuations by a uniform maximum velocity ($U_{max}(x/L = 0.64)$) and the plate distance z by the total height of the cell H. The results at the measurement positions A*, C*, D* are plotted in Figs. 11(a)-11(c). There is a clear difference of the velocity fluctuations in the three flow regions. In flow region 1, both the maxima of the horizontal velocity fluctuations exceed the mean velocity and collapse with the fluctuations of the wall normal component at the location of $z \approx 2\delta_{99\%}$. This indicates fully developed turbulence with the consequence that the local heat transfer coefficient is significantly higher than in the other two flow regions (for a more detailed discussion see Ref. 34). With the evolution of the shear layer in flow region 2, the velocity fluctuations generally decrease to about one third of the values at $x/L = 0.64$ while they grow again close to the opposite sidewall implying further variations in the local heat transfer coefficient.

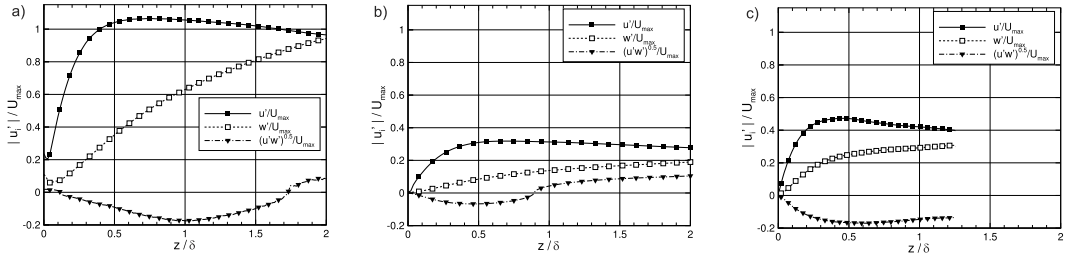

FIG. 11. Profiles of the velocity fluctuations $|u'|$, $|w'|$ and the time-averaged Reynolds stress $(u'w')^{0.5}$ normalized by the maximum velocity at the center of the heating plate at various measurement positions A* (a), C* (b), D* (c).

This physical picture of the evolution of the boundary layer along the path of a single convection roll in a narrow sample can certainly be generalized as well to RB cells of universal geometry, no matter whether only a single roll or multiple rolls exist. In the latter case, the corners of the cell might be replaced by points of vanishing wall shear stress. Those points exist in between the convection rolls where the flow orientation is either towards or off the plate surface. At these areas, both the flow field as well as the local heat transfer coefficient deviate from those areas where the flow is shearing the plate surface. It is conceivable that the ratio between these areas of vanishing wall shear stress and those areas of distinct shear flow changes with respect to the aspect ratio, the Ra number and the Prandtl number and that this variation also may affect the global scaling $Nu(\Gamma, Ra, Pr)$.

IV. CONCLUSION

Highly resolved measurements of the flow field in turbulent Rayleigh-Bénard convection in air have been undertaken using 2D2C particle image velocimetry. In particular, we have focused on the flow field near the lower horizontal plate. Velocity data have been acquired in a vertical plane of about 70 mm height over the entire length of the plate surface. We could identify three different flow regions along the path of the single convection roll being established in the rectangular test sample: (i) a region of wall-normal impingement of the downward flow close to one corner of the sample, (ii) a region where a shear layer with almost constant thickness evolves, and (iii) a region in which this boundary layer grows and eventually detaches from the plate surface at the opposite corner of the sample. The first region that covers about 13% of the total area of the plate surface is characterized by the mainly wall-normal orientation of the flow and a strong mixing of the near-wall flow field. This is accompanied by an enhanced local heat transfer coefficient and also by a different scaling exponent in relation $Nu \sim Ra^{\gamma}$.[35] The second region that covers the major fraction of the plate surface can be considered as a shear flow but unlike in the classical model of a zero-pressure-gradient boundary layer its thickness remains almost constant. It could be confirmed that the shear layer region is clearly in a transitional state to turbulence though the shear Reynolds number Re_{δ_ν} is far below the stability limit of ~420 that has been derived by Tollmien for the classical Prandtl-Blasius boundary layer.[15] In the third flow region starting at about $x/L = 0.88$, the boundary layer grows and eventually detaches from the plate surface. Secondary flow structures that arise out of this detachment may also enhance the local heat transfer coefficient. It might be a future task to investigate whether the sidewall effects that do not appear in turbulent Rayleigh-Bénard convection at large aspect ratio have to be considered when measuring the $Nu \sim Ra^{\gamma}$ scaling in small aspect ratio samples.

ACKNOWLEDGMENTS

We wish to acknowledge the support of the German Research Foundation under the Grant No. PU436/1-2 and the European Union under the Grant Agreement No. 312778. Moreover, we thank Christian Resagk and Robert Kaiser for their valuable scientific contributions and Vigimantas Mitschunas, Sabine Abawi, and Klaus Henschel for the technical assistance to run the experiment.

[1] R. H. Kraichnan, "Turbulent thermal convection at arbitrary Prandtl number," Phys. Fluids **5**, 1374–1389 (1962).
[2] B. Castaing, G. Gunaratne, F. Heslot, L. Kadanoff, A. Libchaber, S. Thomae, X.-Z. Wu, S. Zaleski, and G. P. Zanetti, "Scaling of hard thermal turbulence in Rayleigh-Bénard convection," J. Fluid Mech. **204**, 1–30 (1989).
[3] X. Chavanne, F. Chillá, B. Chabaud, B. Castaing, and B. Hébral, "Turbulent Rayleigh-Bénard convection in gaseous and liquid He," Phys. Fluids **13**, 1300–1320 (2001).
[4] J. J. Niemela and K. R. Sreenivasan, "Confined turbulent convection," J. Fluid Mech. **481**, 355–384 (2003).
[5] X. He, D. Funfschilling, H. Nobach, E. Bodenschatz, and G. Ahlers, "Transition to the ultimate state of turbulent Rayleigh-Bénard convection," Phys. Rev. Lett. **108**, 024502 (2012).
[6] P. Urban, P. Hanzelka, V. Musilová, T. Králik, M. L. Mantia, A. Srnka, and L. Skrbek, "Heat transfer in cryogenic helium gas by turbulent Rayleigh-Bénard convection in a cylindrical cell of aspect ratio 1," New J. Phys. **16**, 053042 (2014).
[7] W. V. R. Malkus, "Discrete transitions in turbulent convection," Proc. R. Soc. London, Ser. A **225**, 185–195 (1954).
[8] W. V. R. Malkus, "The heat transport and spectrum of thermal turbulence," Proc. R. Soc. London, Ser. A **225**, 196–212 (1954).

[9] B. I. Shraiman and E. D. Siggia, "Heat transport in high-Rayleigh-number convection," Phys. Rev. A **42**, 3650–3653 (1990).
[10] S. Grossmann and D. Lohse, "Scaling in thermal convection: A unifying theory," J. Fluid Mech. **407**, 27–56 (2000).
[11] S. Grossmann and D. Lohse, "Multiple scaling in the ultimate regime of thermal convection," Phys. Fluids **23**, 045108 (2011).
[12] Q. Zhou and K.-Q. Xia, "Measured instantaneous viscous boundary layer in turbulent Rayleigh-Bénard convection," Phys. Rev. Lett. **104**, 104301 (2010).
[13] R. du Puits, C. Resagk, and A. Thess, "Thermal boundary layers in turbulent Rayleigh-Bénard convection at aspect ratios between 1 and 9," New J. Phys. **15**, 013040 (2013).
[14] R. du Puits, L. Li, C. Resagk, A. Thess, and C. Willert, "Turbulent boundary layer in high Rayleigh number convection in air," Phys. Rev. Lett. **112**, 124301 (2014).
[15] W. Tollmien, "Ueber die Entstehung der Turbulenz," 1. Mitteilung, Nachr. Ges. Wiss. Goettingen, Math. Phys. Klasse 21–44 (1929).
[16] H. Schlichting, "Zur Entstehung der Turbulenz bei der Plattenstroemung," Nachr. Ges. Wiss. Goettingen, Math. Phys. Klasse 181–208 (1933).
[17] R. du Puits, C. Resagk, and A. Thess, "Measurements of the instantaneous local heat flux in turbulent Rayleigh-Bénard convection," New J. Phys. **12**, 075023 (2010).
[18] Q. Zhou, R. J. A. M. Stevens, K. Sugiyama, S. Grossmann, D. Lohse, and K.-Q. Xia, "Prandtl-Blasius temperature and velocity boundary-layer profiles in turbulent Rayleigh-Bénard convection," J. Fluid Mech. **664**, 297–312 (2010).
[19] R. du Puits, C. Resagk, and A. Thess, "Structure of viscous boundary layers in turbulent Rayleigh-Bénard convection," Phys. Rev. E **80**, 036318 (2009).
[20] N. S. L. Li, R. du Puits, C. Resagk, J. Schumacher, and A. Thess, "Boundary layer analysis in turbulent Rayleigh-Bénard convection in air: Experiment versus simulation," Phys. Rev. E **86**, 026315 (2012).
[21] M. van Reeuwijk, H. J. J. Jonker, and K. Hanjalić, "Wind and boundary layers in Rayleigh-Bénard convection. II. Boundary layer character and scaling," Phys. Rev. E **77**, 036312 (2008).
[22] J. D. Scheel, E. Kim, and K. R. White, "Boundary layer structure in turbulent Rayleigh-Bénard convection," J. Fluid Mech. **711**, 281–305 (2012).
[23] N. Shi, M. S. Emran, and J. Schumacher, "Boundary layer structure in turbulent Rayleigh-Bénard convection," J. Fluid Mech. **706**, 5–33 (2012).
[24] D. Funfschilling and G. Ahlers, "Plume motion and large-scale circulation in a cylindrical Rayleigh-Bénard cell," Phys. Rev. Lett. **19**, 194502 (2004).
[25] H.-D. Xi, S.-Q. Zhou, Q. Zhou, T.-S. Chan, and K.-Q. Xia, "Origin of the temperature oscillation in turbulent thermal convection," Phys. Rev. Lett. **102**, 044503 (2009).
[26] E. Brown and G. Ahlers, "The origin of oscillations of the large-scale circulation of turbulent Rayleigh-Bénard convection," J. Fluid Mech. **638**, 383–400 (2009).
[27] See supplementary material at http://dx.doi.org/10.1063/1.4947261 for the visualization of the flow adjacent to the heated buttom plate at $Ra = 1.45 \times 10^{10}$.
[28] H. Blasius, "Grenzschichten in Fluessigkeiten mit kleiner Reibung," Z. Math. Phys. **56**, 1–37 (1908).
[29] P. Schlatter, R. Örlü, Q. Li, G. Brethouwer, J. H. M. Fransson, A. V. Johansson, P. H. Alfredsson, and D. S. Henningson, "Turbulent boundary layers up to $Re_\theta = 2500$ studied through simulation and experiment," Phys. Fluids **21**, 051702 (2009).
[30] A. Schröder, D. Schanz, R. Geisler, S. Gesemann, and C. Willert, "Near-wall turbulence characterization using 4D-PTV shake-the-box," in *11th International Symposium on Particle Image Velocimetry–PIV15* (Santa Barbara, CA, USA, 2015).
[31] J. Bailon-Cuba, M. S. Emran, and J. Schumacher, "Aspect ratio dependence of heat transfer and large-scale flow in turbulent convection," J. Fluid Mech. **655**, 152–173 (2010).
[32] C. Sun, L.-Y. Ren, H. Song, and K.-Q. Xia, "Heat transport by turbulent Rayleigh-Bénard convection in 1 m diameter cylindrical cells of widely varying aspect ratio," J. Fluid Mech. **542**, 165–174 (2005).
[33] O. Shishkina, S. Wagner, and S. Horn, "Influence of the angle between the wind and the isothermal surfaces on the boundary layer structures in turbulent thermal convection," Phys. Rrev. E **89**, 033014 (2014).
[34] R. Kaiser and R. du Puits, "Local wall heat flux in confined thermal convection," Int. J. Heat Mass Transfer **73**, 752–760 (2014).
[35] R. Kaiser, "Waermestromverteilung in turbulenter Rayleigh-Bénard konvektion," Ph.D. thesis, Technische Universitaet Ilmenau, 2015.